Microscopic origin of the electric Dzyaloshinskii-Moriya interaction

Peng Chen,[1] Hong Jian Zhao,[2,3,1,*] Sergey Prosandeev,[1] Sergey Artyukhin,[4] and Laurent Bellaiche[1,†]

[1]*Physics Department and Institute for Nanoscience and Engineering, University of Arkansas, Fayetteville, Arkansas 72701, USA*

[2]*International Center for Computational Method and Software (ICCMS), Jilin University, 2699 Qianjin Street, Changchun 130012, China*

[3]*Key Laboratory of Physics and Technology for Advanced Batteries (Ministry of Education), College of Physics, Jilin University, Changchun 130012, China*

[4]*Quantum Materials Theory, Istituto Italiano di Tecnologia, 16163 Genova, Italy*

(Received 18 March 2022; revised 14 November 2022; accepted 18 November 2022; published 5 December 2022)

The microscopic origin of the electric Dzyaloshinskii-Moriya interaction (eDMI) is unveiled and discussed by analytical analysis and first-principles based calculations. As similar to the magnetic Dzyaloshinskii-Moriya interaction (mDMI), eDMI also originates from the electron-mediated effect and more specifically from certain electron hoppings that are being activated due to certain local inversion-symmetry breaking. However, the eDMI energy is found to be at least a third-order interaction in atomic displacements instead of bilinear in magnetic dipole moments for mDMI. Furthermore, the eDMI energy form is presented, and we find that novel electrical topological defects (namely, chiral electric bobbers) can arise from this eDMI. Thus unraveling the microscopic origin of eDMI has the potential to lead to, and explain, the discovery of novel polar topological phases.

DOI: 10.1103/PhysRevB.106.224101

I. INTRODUCTION

The seminal works that addressed and explained the magnetic Dzyaloshinskii-Moriya interaction (DMI) were done in 1957 and 1960 by Dzyaloshinskii [1,2] and Moriya [3], and named after them. Dzyaloshinskii first pointed out the existence of the antisymmetric form of interaction by symmetry analysis. Moriya then derived the microscopic origin of the magnetic Dzyaloshinskii-Moriya interaction (mDMI) by considering the spin-orbit coupling (SOC) and taking electron hopping as perturbation. mDMI revolutionized magnetism, since it, e.g., explains nontrivial noncollinear topological textures such as vortices [4,5], skyrmions [6–19], and domain walls [20,21], which is intriguing for both fundamental theory and potential applications.

Magnetic effects normally have their electric analog counterpart which is deep-rooted in electromagnetic theory. Strikingly, despite the fact that ferroelectric vortices and skyrmions have been recently reported in superlattices made of ferroelectric $Pb(Zr,Ti)O_3$ or $PbTiO_3$ sandwiched by either paraelectric $SrTiO_3$ dielectric layers [22–26] or $SrRuO_3$ metallic layers [27], after having been predicted [28–30], it was not clear until recently whether an electric analog of mDMI exists. As a matter of fact, such exotic orders of electric dipoles were typically explained by electrostatic boundary conditions [31] rather than by considering the electric Dzyaloshinskii-Moriya interaction (eDMI). Recent symmetry analysis and *ab initio* calculations by Zhao *et al.* [32] and the observation of helical textures of electric dipoles [33] in bulk perovskites (which are systems for which there is no depolarization field) have changed such perception. The discovery of eDMI not only should deepen our knowledge of electromagnetic phenomena (e.g., magnetic noncollinear spins versus electric noncollinear dipole patterns), but is also of technological importance. For example, mDMI generally plays an primordial role in generating magnetic topological phases (e.g., helimagnets [34–36], skyrmions [6–19], and merons [18,37,38]). These magnetic topological phases have potential applications in designing logical/storage devices based on magnetic fields or electric currents. However, challenges still exist for magnetic topological defects [39,40], which are that (1) the size of these defects, such as magnetic skyrmions, needs to be scaled down from micrometer (or 100 nm) to nanometers; (2) topological defects like magnetic skyrmions usually need an external magnetic field to assist their stability and the temperature at which they exist can be rather low; and (3) the response velocity of the magnetic topological phases under external field (especially electric field/current) needs to be improved. The discovery of possible electric topological phases (e.g., the electric counterpart of mDMI-based helical electric polar structures [33], electric polar skyrmions [24,30], and electric polar vorticies [22,23,25–27]) has the potential to overcome these drawbacks, since (i) the observed electric topological phases are in nanometer scale and many have been reported at room temperature [22–27,33]; (ii) an electric field control of dipole textures would avoid the Joule heating (and thus leads to low-power devices) [39]; and (iii) electric dipole textures normally have a fast response to the electric field. Moreover, from a fundamental physical knowledge viewpoint, the discussion of an intrinsic eDMI term that could stabilize the above-mentioned topological defects has long been overlooked when studying ferroelectric/polar materials, until recent *ab initio* calculations [32] clearly indicated its existence.

*physzhaohj@jlu.edu.cn
†laurent@uark.edu

Let us recall that in Ref. [32], phenomenological models revealed a sequence of trilinear couplings, which showcase the existence of eDMI coming from oxygen octahedral rotations. However, many important ferroelectric materials (such as $PbTiO_3$ and $KNbO_3$) do not have any oxygen octahedral tiltings and, as will be shown in this paper, they do possess eDMI. One may thus wonder if there is a general theory to explain the eDMI from a microscopic point of view and if the previously found oxygen-octahedral-tiling-mediated eDMI is only a special case. In this paper, we aim at addressing the microscopic origin of such an eDMI and answering several important open questions: (i) What is the microscopic origin of eDMI energy which gives rise to a cross-product form of ionic displacements $\boldsymbol{u}_i$ and $\boldsymbol{u}_j$:

$$\boldsymbol{\mathcal{D}}(i,j)\cdot(\boldsymbol{u}_i\times\boldsymbol{u}_j), \tag{1}$$

where $\boldsymbol{\mathcal{D}}(i,j)$ is the eDMI vector? (ii) Is eDMI a classical or quantum effect? (iii) What is the energy scale of the eDMI? Practically, bulk $PbTiO_3$ is selected as a study platform. We first show that eDMI can be obtained by extracting the antisymmetric part of the force constants. Then, a Green's function perturbation method in a tight-binding (TB) electron Hamiltonian is adopted to study the origin of such antisymmetric feature. By carefully looking into the forces coming from different orbital hopping channels, we then find that a similar mechanism that gives rise to mDMI also happens in ferroelectric materials and thus induces eDMI. More specifically, we discover that (1) certain local inversion-symmetry breaking activates forbidden electron hopping channels on adjacent atomic sites; and (2) it is the combination of the orbitals following certain selection rules that results in the antisymmetric form of forces and thus eDMI. We also provide an analytical form of the eDMI energy in perovskite materials, as well as compute its coefficient which is estimated to be only one order smaller than that of the typical energy that favors collinear polar texture. Consequently, noncollinear arrangements resulting from this eDMI have the potential to occur and be observed.

II. FORMALISM

A. Antisymmetric force constants and eDMI

The ferroelectric polarization can be characterized by a collection of atomic displacements. Taking $PbTiO_3$ as in Fig. 1(a) for example, the first-principles calculated normalized polar mode (which is soft in the cubic structure) consists of titanium and lead cations displaced by 0.78 and 0.31 Å along the positive z direction, respectively; the oxygen anions that are on the side of titanium ions within (001) planes being displaced by 0.38 Å in the negative z direction; and the oxygen anions that align with titanium ions along the z axis being vertically displaced by 0.08 Å in the positive z direction. Considering that the titanium cation has the largest displacement and is parallel to the total polarization, we use here the force constants [41] between titanium sites to study qualitatively the force constants of polarization [42] (note that experiments also use atomic displacements, such as those of titanium and lead ions, to visualize noncollinear dipolar configurations [22,24,25], which is another reason we use the force constants of specific ionic sites). In the purpose of studying eDMI, we extract

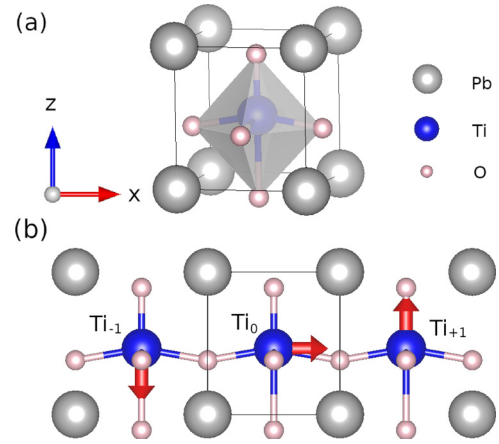

FIG. 1. (a) Tetragonal phase of $PbTiO_3$, with titanium ions displaced along the z direction. (b) Illustrative plot of some atomic displacements under certain force constants $F_{\alpha\beta}(i,j)$ between titanium pairs with $i=\mathrm{Ti}_0$ and $j=\mathrm{Ti}_{+1}$ along the x direction: $F_{xz}(\mathrm{Ti}_0,\mathrm{Ti}_{+1})$ and $F_{zx}(\mathrm{Ti}_0,\mathrm{Ti}_{+1})$. Note that $F_{zx}(\mathrm{Ti}_{-1},\mathrm{Ti}_0)$ is equal to $F_{zx}(\mathrm{Ti}_0,\mathrm{Ti}_{+1})$ due to the translational symmetry along the x direction. The red vectors illustrate one possible set of the atomic displacement pattern that could result from a negative $F_{xz}(\mathrm{Ti}_0,\mathrm{Ti}_{+1})$ and positive $F_{zx}(\mathrm{Ti}_0,\mathrm{Ti}_{+1})$.

the antisymmetric part of the force constant matrix between different sites i and j via

$$\|F^A(i,j)\|=\tfrac{1}{2}(\|F(i,j)\|-\|F(i,j)\|^{\mathrm{T}}), \tag{2}$$

where T is the matrix transpose operation, $\|F(i,j)\|$ is the force constant matrix between sites i and j, and the achieved $\|F^A(i,j)\|$ is antisymmetric as it satisfies $\|F^A(i,j)\|=-\|F^A(i,j)\|^{\mathrm{T}}$. As detailed in Sec. I of the Supplemental Material [43] (see, also, Refs. [44–55,55–57,57–65] therein), it is the antisymmetric part of force constants that gives rise to the energy as in Eq. (1) and defines the eDMI vector $\boldsymbol{\mathcal{D}}(i,j)$ via

$$\boldsymbol{\mathcal{D}}(i,j)=\left(F^A_{y,z},F^A_{z,x},F^A_{x,y}\right), \tag{3}$$

where $F^A_{y,z}=(F_{y,z}-F_{z,y})/2$, $F^A_{z,x}=(F_{z,x}-F_{x,z})/2$, $F^A_{x,y}=(F_{x,y}-F_{y,x})/2$, and the Cartesian directions of x, y, and z are used here to indicate matrix entries of the force constant matrix. Note also that, by the antisymmetric part of force constants, we mean the force constant matrix between a pair of ions rather than the overall force constant matrix that contains all ions, since such latter force constant matrix is always symmetric [41].

B. Orbital-resolved force constants

Normally, density functional perturbation theory (DFPT) takes the variation of electron density with respect to the ionic displacements and calculates the force constants in self-consistent processes. Though higher-order corrections can be included, the physical insight is missing. For example, it does not reveal which orbital specifically contributes to the force constants and how it results in an antisymmetric character. Alternatively, we thus decided to use a perturbation method derived from a tight-binding (TB) Hamiltonian to calculate the antisymmetric part of the force constants, which allows

us to analyze orbital-resolved force constants. The details of this method can be found in Refs. [53,54] and have also been summarized in Sec. IV of the Supplemental Material [43]. Interestingly, a similar formalization has been previously used to calculate the magnetic exchange parameters [57,60,62] $J_{\alpha\beta}(i,j)$ which can be seen as "force constants" of spins and whose antisymmetric part corresponds to mDMI. The only difference between calculating $J_{\alpha\beta}(i,j)$ and $F_{\alpha\beta}(i,j)$ is that instead of taking ionic displacement as perturbation, $J_{\alpha\beta}(i,j)$ takes spin rotations. Such formalism has also recently been used to explain mDMI in the trihalides $CrCl_3$ and CrI_3 [66], Mn_3Sn [67], and clusters of $3d$ metals [68].

As detailed in Sec. IV of the Supplemental Material [43], the force constants $F_{\alpha\beta}(i,j)$ can be written as integration of force constant density [53,54] $f_{\alpha,\beta}(\varepsilon,i,j)$ as

$$F_{\alpha\beta}(i,j)=\int_{-\infty}^{\varepsilon_f} f_{\alpha,\beta}(\varepsilon,i,j)d\varepsilon \tag{4}$$

in which

$$f_{\alpha,\beta}(\varepsilon,i,j)=\sum_{m,n}\xi_{\alpha,\beta}^{m,n}(\varepsilon,i,j), \tag{5}$$

where the orbital-resolved force constant density $\xi_{\alpha,\beta}^{m,n}$ can be further written as

$$\xi_{\alpha,\beta}^{m,n}(\varepsilon,i,j) = -\frac{1}{2\pi}\mathrm{Im}[\langle m,i|U_{i,\alpha}\hat{G}^0(\varepsilon)U_{j,\beta}|n,j\rangle\langle n,j|\hat{G}^0(\varepsilon)|m,i\rangle], \tag{6}$$

where U are effective perturbation potentials as defined in Sec. IV of the Supplemental Material [43] and in Ref. [53]. Note that $U_{i,\alpha}$ is taken here as a short notation of $\frac{\partial U}{\partial\tau_{i,\alpha}}$, where $\boldsymbol{\tau}$ is the ionic position of site i. The Green's function operator $\hat{G}^0(\varepsilon)$ is defined as $\sum_p \frac{|p\rangle\langle p|}{\varepsilon-\varepsilon_p+i\eta}$, where ε_p and $|p\rangle$ are the energy and wave function in the unperturbed system H^0; Im is the operation to take the imaginary part. Since the total force constants of Eq. (4) are calculated by integrating $f_{\alpha,\beta}(\varepsilon,i,j)$, these latter are called the force constants' density as a function of energy ε. Equation (5) defines $\xi_{\alpha,\beta}^{m,n}(\varepsilon,i,j)$ as orbital-resolved force constant density from orbital m on site i and orbital n on site j, and the summations of $\xi_{\alpha,\beta}^{m,n}(\varepsilon,i,j)$ over orbitals m and n gives rise to force constant density $f_{\alpha,\beta}(\varepsilon,i,j)$ in see Eq. (5). Employing Eq. (4) in Eq. (3), the $\boldsymbol{\mathcal{D}}$ vector can be rewritten in force constant density expressions as

$$\boldsymbol{\mathcal{D}}(i,j)=(\mathcal{D}_x(i,j),\mathcal{D}_y(i,j),\mathcal{D}_z(i,j)), \tag{7}$$

where

$$\mathcal{D}_x(i,j)=\frac{1}{2}\int_{-\infty}^{\varepsilon_f}[f_{y,z}(\varepsilon,i,j)-f_{z,y}(\varepsilon,i,j)]d\varepsilon, \tag{8}$$

$$\mathcal{D}_y(i,j)=\frac{1}{2}\int_{-\infty}^{\varepsilon_f}[f_{z,x}(\varepsilon,i,j)-f_{x,z}(\varepsilon,i,j)]d\varepsilon, \tag{9}$$

$$\mathcal{D}_z(i,j)=\frac{1}{2}\int_{-\infty}^{\varepsilon_f}[f_{x,y}(\varepsilon,i,j)-f_{y,x}(\varepsilon,i,j)]d\varepsilon. \tag{10}$$

Detailed derivations for reproducing the orbital-resolved force constant density as in Refs. [53,54] can be found in Sec. IV the Supplemental Material [43].

C. Numerical details

For the numerical calculation, we use the symmetry-adapted Wannier basis [69] for the TB Hamiltonian. The Wannierization is performed using Wannier90 [70] and Quantum Espresso [71,72] to extract all the following orbitals of Ti : $4s^1, 3p^3, 3d^5$, Pb : $6s^1, 6p^3, 5d^5$, and O : $2s^1, 2p^3$, 30 Wannier functions in total. Note that each Wannier function is twofold degenerated since we are working with a spin-nonpolarized situation. The core electrons are treated as tightly bound to the nucleus by optimized norm-conserving Vanderbilt pseudopotentials [73]. The Green's function $G^0(\varepsilon,\boldsymbol{k})$ is calculated by numerically inverting $(\varepsilon+\varepsilon_f)\mathrm{I}-H^0(\boldsymbol{k})$, where H^0 is the TB Hamiltonian of the unperturbed structure, I is an identity matrix, ε_f is the Fermi energy level from the self-consistent first-principle calculation, and $\boldsymbol{k}$ is the Bloch vector defined in the first Brillouin zone. Fourier transformation can then be used to determine the Green's function in real space $G^0(\varepsilon,i,j)$. The bare potential V^b, Hartree potential V_h, and exchange correlation potential V_{xc} are extracted from self-consistent first-principles calculations in order to evaluate the $\tilde{U}$ and U^b following the definitions in Sec. IV of the Supplemental Material [43]. The perturbation is induced by shifting both the ionic potentials and Wannier functions by 0.15 Å, numerically. Since the Wannier functions are predefined in real space on a coarse grid, the displacements of Wannier functions need to be performed in reciprocal space first and then transformed back. The finite-difference method is used to obtain the partial derivatives $\frac{\partial U}{\partial\tau_{i,\alpha}}$. Furthermore, the integration of the complex energy in Eq. (4) is performed over a rectangular contour. The η in the Green's function is chosen to be 0.1 eV, such that the evaluation of $-\frac{1}{\pi}\mathrm{ImTr}[G^0(\varepsilon,0,0)]$ in the original crystal cell ($i=0$ and $j=0$) reproduces nicely the same density of states as calculated from first-principles calculations. The plane-wave energy cutoffs for wave function and electron density are 50 and 400 Ry, respectively, in Quantum Espresso. A k mesh of $9\times9\times8$ is used in the first-principles self-consistent calculations and a q mesh of $4\times4\times4$ is used in the DFPT force constant calculations.

III. THE EXISTENCE OF eDMI

Note that eDMI was not thought to exist until the recent work [32] by Zhao *et al.* that changed such perception by demonstrating that it is allowed by symmetry. Note also that the phenomenological mechanism discussed by Zhao *et al.* includes oxygen octahedral tiltings and complex energy forms. However, the eDMI should exist even in systems that do not have oxygen octahedral tiltings, such as $PbTiO_3$. Such fact suggests that there could exist other and possibly simpler microscopic explanations of eDMI.

A. Intrinsic eDMI in bulk

When performing DFPT calculations on the $PbTiO_3$ tetragonal phase [as depicted in Fig. 1(a) in which the polarization is along the z direction], we found that the antisymmetric part of the force constants between titanium sites being nearest neighbors along the x direction is a matrix $\|F^A(i,j)\|$ having

the following elements:

$$\|F^A(i,j)\| = \begin{pmatrix} 0 & 0 & -0.73 \\ 0 & 0 & 0 \\ 0.73 & 0 & 0 \end{pmatrix}, \tag{11}$$

where the matrix entries go through the Cartesian $\{x, y, z\}$ directions, and i and j are used to indicate the nearest-neighbor pair of the titanium sites along the x direction, such as between Ti_{-1} and Ti_0 or Ti_0 and Ti_{+1} in Fig. 1(b). Consequently, the $\boldsymbol{\mathcal{D}}(i,j)$ vector, according to Eq. (3), involving first nearest neighbors along the x axis of $PbTiO_3$ is equal to (0,0.73,0) which favors titanium atoms to be displaced anticlockwise, as shown in Fig. 1(b). On the other hand, when calculating the $\|F^A(i,j)\|$ in the case of the polarization direction being reversed, the calculated $\boldsymbol{\mathcal{D}}(i,j)$ vector is found to reverse to $(0,-0.73,0)$, which favors titanium atoms to be displaced clockwise. Note that the off-diagonal value 0.73 eV/Å^2 is only one-quarter of the largest component of the symmetric part of force constants $\|F^S(i,j)\|_{x,x} = -2.84$ and even a little bit larger in the absolute value than $\|F^S(i,j)\|_{y,y} = -0.64$ and $\|F^S(i,j)\|_{z,z} = -0.66$, which suggests a strong competition between the collinear coupling decided by the symmetric part of the force constants and the noncollinear coupling decided by the antisymmetric part of the force constants. Note also that in the famous bulk/interfacial mDMI pictures [74], the magnetic interaction between two neighboring ions and a single third ion (ligand) is the minimal model [40,75,76] to discuss the mDMI. For example, in ABO_3 perovskites, the mDMI is usually rooted in neighboring B-O-B pairs (e.g., the mDMI of Fe-O-Fe pairs in $BiFeO_3$). To understand the microscopic origin of eDMI in a way resembling the situation of the mDMI, we start from the B-B pairs (e.g., Ti-Ti pairs in our model system $PbTiO_3$). Noteworthy is that such an eDMI is not limited to Ti-Ti pairs, but is also valid for Pb-Pb pairs. The calculated eDMI for the nearest-neighboring Pb-Pb pair, given by the $\boldsymbol{\mathcal{D}}(i,j)$, is (0,0.075,0), which favors A-site Pb to be displaced anticlockwise looking from the positive y direction. Moreover, when calculating the $\boldsymbol{\mathcal{D}}(i,j)$ vector for polar modes that contain contributions from all atoms (Pb, Ti, and O), a unitary transformation was performed on the whole force constant matrix [77].

B. Coupling form and scale of eDMI

In order to determine the energetic coupling form that can give rise to the eDMI vector, we take the centrosymmetric $Pm\bar{3}m$ phase as reference and look for the energy invariants written in terms of the displacements $\boldsymbol{u}$. The third-order terms are found to be the lowest order that can give rise to antisymmetric force constants. Actually, the derived energy term associated with the polar modes on the nearest-neighbor sites should always be in odd number of orders and the third order is therefore the minimal requirement. This is because all $\boldsymbol{u}_i$, $\boldsymbol{u}_j$, and $\boldsymbol{e}_{ij}$ (vector that is pointing from site i to j) reverse sign under inversion operation, which means that at least an extra odd order of $\boldsymbol{u}_i$ or $\boldsymbol{u}_j$ needs to be included to make the energy term invariant under inversion symmetry [78]. Thus a bilinear form as in Eq. (1) with respect to polar modes is forbidden by symmetry, if $\boldsymbol{\mathcal{D}}(i,j)$ does not depend on the $\boldsymbol{u}$ displacements. Assuming the eDMI to adopt the same form as the second-order mDMI [79] may not be valid in some materials. In fact, by symmetry analysis, we find there exists only one third-order eDMI energy and it can be written in compact form:

$$E_{dmi} = \mathcal{A}^-[(\boldsymbol{u}_i + \boldsymbol{u}_j) \times \boldsymbol{e}_{ij}] \cdot (\boldsymbol{u}_i \times \boldsymbol{u}_j), \tag{12}$$

where $\mathcal{A}^-$ is constant and $\mathcal{A}^-(\boldsymbol{u}_i + \boldsymbol{u}_j) \times \boldsymbol{e}_{ij}$ is the eDMI $\boldsymbol{\mathcal{D}}(i,j)$ vector. Note that we numerically found from DFT calculations on the ferroelectric tetragonal phase of $PbTiO_3$ that the magnitude of the eDMI vector $\mathcal{A}^-(\boldsymbol{u}_i + \boldsymbol{u}_i) \times \boldsymbol{e}_{ij}$ is 7.65×10^6 Nm^2/C^2. Note that Eq. (12) is the pure chiral part (giving rise to antisymmetric forces) of the energy that is itself derived from two energy invariants (that can be found in Sec. VI of the Supplemental Material [43]). An equivalent expression that is written in atomistic displacement basis is also presented in Secs. VI B and C of the Supplemental Material [43], in order to see the roles from individual atoms.

It is also interesting to realize that the spin current model [80,81] gives a mDMI for which the energy is proportional to $(\boldsymbol{u}_i \times \boldsymbol{e}_{ij}) \cdot (\boldsymbol{m}_i \times \boldsymbol{m}_j)$, and thus for which the mDMI vector is proportional to $(\boldsymbol{u}_i \times \boldsymbol{e}_{ij})$. Such latter vector is very similar to the eDMI vector $\mathcal{A}^-(\boldsymbol{u}_i + \boldsymbol{u}_j) \times \boldsymbol{e}_{ij}$ [see Eq. (12)], which shows again an essential connection between magnetism and electricity. Note that the spin current model assumes homogeneous dipole moments; thus $\boldsymbol{u}_i$ there is equal to $(\boldsymbol{u}_i + \boldsymbol{u}_j)/2$. On the other hand, Eq. (12) emphasizes that eDMI energy is third order with respect to the ionic displacements, while mDMI in the spin-current model is bilinear with respect to magnetic moments and linear with respect to the ionic displacement.

The calculated nonzero $\boldsymbol{\mathcal{D}}(i,j)$ vector in bulk $PbTiO_3$ suggests that, in addition to the depolarization field, another intrinsic mechanism involving now this kind of force constant can also contribute to the formation of polar vortices observed, e.g., in $PbTiO_3/SrTiO_3$ superlattices [22,24,25] and especially in $PbTiO_3/SrRuO_3$ superlattices [27] (because the metallic $SrRuO_3$ layers can result in much weaker depolarization field).

C. Chiral electric bobbers from eDMI

It is interesting and important to know what type of dipolar structures one should expect from Eq. (12). Thus we took the traditional effective Hamiltonian model for $PbTiO_3$ (see Supplemental Material [43] Sec. VII for details) and additionally considered the eDMI energy in Eq. (12) to explore such possible electric defects. When we increase the magnitude of coefficient $\mathcal{A}^-_{nn}$ (nearest neighbor) and $\mathcal{A}^-_{nnn}$ (next-nearest neighbor) in front of Eq. (12) from -0.001021 hartrees/bohr^3 and -0.000353 hartrees/bohr^3 (fitted for PTO) to values larger than -0.001813 hartrees/bohr^3 and -0.000544 hartrees/bohr^3, respectively, chiral electric bobbers (the electric counterpart of the ones in magnetic systems [82–86]) emerge, as depicted in Figs. 2(a) and 2(b). The electric bobber survives only on the top surface of a monodomain with polarization pointing downward, and its chirality is decided by the sign of the coefficient $\mathcal{A}^-$ of Eq. (12). As can be seen from Fig. 2(b), the up dipoles (on the edge of the blue region) rotate clockwise on the surface layer along the y direction, due to a negative eDMI vector with respect to

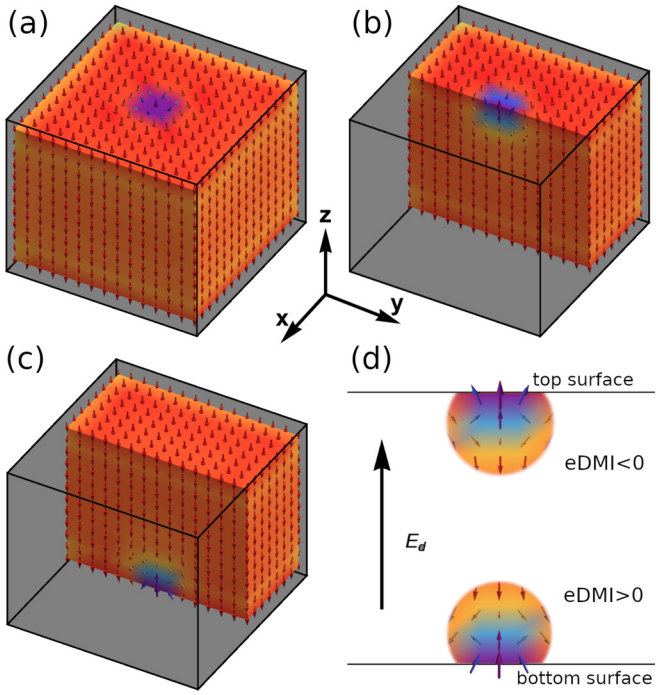

FIG. 2. (a) Top view of the surface bubble defect achieved with negative eDMI. (b) Cross-section view of the (top) surface bubble defect from negative eDMI. (c) Cross-section view of the (bottom) surface bubble defect from positive eDMI. (d) Schematic illustration to show the charge and chirality of the surface bubble defects with respect to the sign of eDMI; the black arrow is to indicate the depolarization field (E_d) direction. In addition, the red domains have polarization along the negative z direction, and the blue domains (defects) have polarization along the positive z direction.

the x axis. When we rather use a positive $\mathcal{A}^-$ (i.e., reverse its sign), the electric bobber now only exists on the bottom surface of the monodomain. Anticlockwise-rotated down dipoles can be seen from Fig. 2(c) (on the edge of the blue region) along the y direction, due to a positive eDMI vector with respect to the x axis. Similarly to the chiral magnetic bobbers, singularities (head-to-head and tail-to-tail dipoles) exist; however, chiral electric bobbers are rather small and are surface-dependent. As illustrated in Fig. 2(d), negative eDMI always gives a clockwise rotation of dipoles on the top surface, while positive eDMI favors the anticlockwise rotation of dipoles on the bottom surface; because of the existence of depolarization field in ferroelectric materials, the electric bobbers are surface-dependent; say bobbers with upward dipoles will locate only on the top surface and bobbers with downward dipoles will locate only on the bottom surface in a ferroelectric monodomain with polarization downward.

Note the strength of eDMI needs to be increased by 78% with respect to its *ab initio* value to achieve such electric defects in PTO, but such resulting larger value may be found in other systems. We also find that such defects do not exist when the film is too thin, e.g., less than 10 unit cells. In addition, though the eDMI is necessary to stabilize electric bobbers, other intrinsic interactions, such as j5 and j7, are also found to be important to stabilize such a metastable phase on the surface. We have also found that eDMI is responsible for the formation of the mixed Ising-Néel type domain walls [87] (see Supplemental Material [43] Fig. 8 for details). Thus it can be seen that the effect of eDMI can result in novel and/or complex textures and, due to the strong dipole-dipole interaction, mainly survives near the surface and domain walls.

IV. MICROSCOPIC ORIGIN OF eDMI

As is well known, mDMI originates from SOC [3]. In contrast, the origin of the calculated eDMI (the antisymmetric force constants) is currently unknown and thus needs to be unsealed. In the following, we will explain the origin of the antisymmetric feature of force constants as shown in Eq. (11) via electron hoppings, which will thus further explain the microscopic origin of eDMI vector $\boldsymbol{\mathcal{D}}_{ij}$ and its dependency on the polarization orientation as in Eq. (12).

A. eDMI as an electron-mediated quantum effect

To determine the origin of eDMI, we decided to look in detail at the microscopic full Hamiltonian [59] (involving both electrons and ions) and derive the potential energy surface and its Hessian matrix. By following the textbook derivation as described in Sec. III of the Supplemental Material [43], the force constant expression from the DFPT can be written as [59]

$$F_{\alpha\beta}(i,j) = \frac{\partial^2 \Omega(\boldsymbol{\tau})}{\partial \tau_{i,\alpha} \partial \tau_{j,\beta}} \tag{13a}$$

$$= \frac{\partial^2 V_{ii}(\boldsymbol{\tau})}{\partial \tau_{i,\alpha} \partial \tau_{j,\beta}} + \int d\boldsymbol{r} \frac{\partial V_{ie}(\boldsymbol{r};\boldsymbol{\tau})}{\partial \tau_{i,\alpha}} \frac{\partial n(\boldsymbol{r};\boldsymbol{\tau})}{\partial \tau_{j,\beta}}. \tag{13b}$$

It thus involves the second derivative of the potential energy surface $\Omega(\boldsymbol{\tau})$ with respect to ionic positions $\boldsymbol{\tau}_i$ and $\boldsymbol{\tau}_j$ ($i \neq j$) (e.g., Ti_0 and Ti_{+1} in Fig. 1) along α and β Cartesian directions, respectively. Note that $n(\boldsymbol{r};\boldsymbol{\tau})$ is the electronic density, while the contribution to the force constant $F_{\alpha\beta}$ is divided into two parts: (1) the energy potential of ion-ion interaction $V_{ii}(\boldsymbol{\tau})$ that includes the nucleus and inner core electrons that rigidly follow the ionic displacements, and (2) ion-electron interaction $V_{ie}(\boldsymbol{r};\boldsymbol{\tau})$ that includes both the ions (nucleus combined with inner core electrons) and valence electrons $n(\boldsymbol{r};\boldsymbol{\tau})$. Since V_{ii} is a sum of repulsive ion-ion Coulomb interactions, the first term of the right side of Eq. (13b) only contributes to the symmetric part of the force constants (see proofs in Sec. II of the Supplemental Material [43]). Thus the antisymmetric form in Eq. (11) has to come from the second term of the right side of Eq. (13b), which in fact can be seen as the electron-density-mediated ion-ion indirect interaction. More specifically, Eq. (13b) indicates that (i) the change of the ionic position $\tau_{i,\alpha}$ induces a variation of electron-ion energy $\frac{\partial V_{ie}(\boldsymbol{r};\boldsymbol{\tau})}{\partial \tau_{i,\alpha}}$ at site i, (ii) which couples to the change of ionic position $\tau_{j,\beta}$ on site j through the electron density fluctuation $\frac{\partial n(\boldsymbol{r};\boldsymbol{\tau})}{\partial \tau_{j,\beta}}$. Thus, though eDMI is mostly associated with ionic dipoles, Eq. (13) tells us that eDMI is not included in the dipole-dipole interaction and, instead of treating electrons as point charges, treating electrons as wave functions is important to obtain eDMI. Thus eDMI originates from an electron-mediated quantum effect. Note that the dipole-dipole interaction that takes consideration of the Born effective charges in a full tensor form should

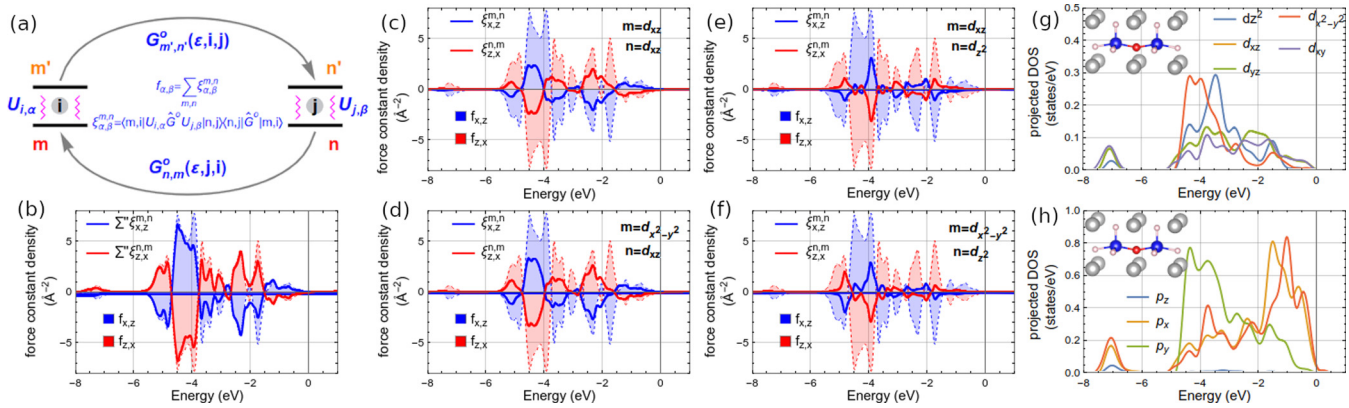

FIG. 3. (a) Diagram plot of orbital-resolved force constant density $\xi^{m,n}_{\alpha,\beta}$ defined as $\sum_{m',n'}\langle m,i|U_{i,\alpha}|m',i\rangle\langle m',i|\hat{G}^0(\varepsilon)|n',j\rangle\langle n',j|U_{j,\beta}|n,j\rangle\langle n,j|\hat{G}^0|m,i\rangle$ (see Eq. (6) and Eq. (32) in Sec. IV of the Supplemental Material [43]). Panels (b), (c), (d), and (e) are plots of orbital-resolved force constant density ($\xi^{m,n}_{x,z}$ in blue line and $\xi^{n,m}_{z,x}$ in red line) and total force constant density [$f_{x,z}(\varepsilon,i,j)$ in blue area and $f_{z,x}(\varepsilon,i,j)$ in red area], as defined in Eqs. (4) and (5). More specifically, panel (c) contains $\xi^{m,n}_{x,z}$ and $\xi^{n,m}_{z,x}$ where $m=d_{xz}$ and $n=d_{xz}$; panel (d) contains $\xi^{m,n}_{x,z}$ and $\xi^{n,m}_{z,x}$ where $m=d_{x^2-y^2}$ and $n=d_{xz}$; panel (e) contains $\xi^{m,n}_{x,z}$ and $\xi^{n,m}_{z,x}$ where $m=d_{xz}$ and $n=d_{z^2}$; panel (f) contains $\xi^{m,n}_{x,z}$ and $\xi^{n,m}_{z,x}$ where $m=d_{x^2-y^2}$ and $n=d_{z^2}$; and panel (b) contains the sum of all the $\xi^{m,n}_{x,z}$ and $\xi^{n,m}_{z,x}$ plotted in panels (c), (d), (e), and (f). Panels (g) and (h) are density of states (DOS) projected on the titanium atom (blue ball in the subset) and oxygen atom (red ball in the inset). Note that the Fermi level is set at the zero of energy in all the plots.

include the eDMI energy because the Born effective changes are associated with the electronic responses to the atomic displacements, which can be seen as another perspective to understand the electrons' role in the eDMI.

In order to further understand the role of the electrons in the eDMI, the orbital-resolved force constants [53,54] need to be calculated. The second-order perturbation is performed to calculate the orbital-resolved force constant density in Eq. (6) and the perturbation process can be summarized as in Fig. 3(a): (i) an atomic displacement $u_{i,\alpha}$ first induces an effective perturbation energy potential change $U_{i,\alpha}$ on site i (left gray ball) and scatters state $|m,i\rangle$ (lower level on the left) to $|m',i\rangle$ (top level on the left); (ii) such scattering is propagated by the Green's function $G^0_{m',n'}(\varepsilon,i,j)$ from site i to site j (gray arrow on the top); and (iii) couples to the atomic displacement $u_{j,\beta}$ on site j (right gray ball) by alternating the effective perturbation potential $U_{j,\beta}$ and scattering state $|n,j\rangle$ (lower level on the right) to $|n',j\rangle$ (top level on the right); (iv) another Green's function $G^0_{n,m}(\varepsilon,j,i)$ (gray arrow in the bottom) closes the "loop" by propagating the scattered state n from site j back to state m on site i. The specific mathematical expression of such loop can be found in Eq. (32) of the Supplemental Material [43] and the more detailed mathematical definitions of $U_{i,\alpha}$, $U_{j,\beta}$, and the Green's functions $G^0_{m',n'}(\varepsilon,j,i)$ and $G^0_{n,m}(\varepsilon,j,i)$ can be found in Sec. IV of the Supplemental Material [43]. Note that the orbital scatterings in Fig. 3(a) as well as Eq. (6) show that the forces between atoms need a quantum treatment by the Hellman-Feynman theorem [47,51]. The eDMI should therefore be a quantum effect since the antisymmetric forces can only come from the interactions between (quantum) electrons and (classical) ions. It is worth mentioning that such loop is physically equivalent to the DFPT process when calculating the force constants from Eq. (13a).

Each loop as in Fig. 3(a) is one contribution to the force constants from a set of orbitals m,m',n', and n. The summation of all the possible loops defined by m,m',n', and n orbitals gives rise to the force constants and can also be calculated by other methods such as DFPT. In our calculations, there are in total 6561 (sum over m,m',n', and n) loops that contribute to the force constants. For the simplicity of further analysis, we define orbital-resolved force constant density $\xi^{m,n}_{\alpha,\beta}(\varepsilon,i,j)$ by summing out the m' and n' in the loops, see Eq. (6), which represents the force constant density contribution from one orbital m on site i and another orbital n on site j to the force constants, where α and β are elements of Cartesian $\{x,y,z\}$ directions, m and n range among all the orbitals on site i and j, respectively, and ε is the energy. The sum of the orbital-resolved force constant density $\xi^{m,n}_{\alpha,\beta}(\varepsilon,i,j)$ over m and n is defined as the force constant density $f_{\alpha,\beta}(\varepsilon,i,j)$, as formulated in Eq. (5). Thus the total force constants, according to Eq. (4), can be obtained by integrating $f_{\alpha,\beta}(\varepsilon,i,j)$ from negative infinite to the Fermi energy at the highest occupied energy level. $F_{x,z}$ and $F_{z,x}$ in Eq. (11) are calculated to be -0.58 and 0.58 eV/Å^2 according to our TB model, respectively, which are comparable to the aforementioned DFPT results of -0.73 eV/Å^2 and 0.73 eV/Å^2. We also calculated the next-nearest neighbor $F_{x,z}$ and $F_{z,x}$ which are -0.16 eV/Å^2 and 0.16 eV/Å^2 according to our TB model, once again in good agreement with DFPT results of -0.14 eV/Å^2 and 0.14 eV/Å^2. Note that the slight discrepancy between TB and DFPT results likely comes from the facts that our TB perturbation drops second- and higher-order electron density fluctuation and assumes a rigid Wannier orbital displacements, while the DFPT includes both the displacement of orbitals and the change of the orbital shapes during the self-consistent process of the electron density response.

So far three quantities are defined and will be used in the future analysis: the summation of (1) the orbital-resolved force constants density $\xi^{m,n}_{\alpha,\beta}(\varepsilon,i,j)$ [see Eq. (6)] over orbital m on site i and n on site j gives rise to (2) the force

constants density $f_{\alpha,\beta}(\varepsilon, i, j)$ [see Eq. (5)], whose integration over energy ε is (3) the force constants $F_{\alpha,\beta}(i, j)$ [see Eq. (4)] between sites i and j.

B. Origin of the antisymmetric feature

The orbital-resolved force constant density $\xi^{m,n}_{\alpha,\beta}$ allows us to analyze the force constant contributions from different orbital combinations between sites i and j. As in Eq. (5), the summation of the orbital-resolved force constant density over all possible m and n orbitals gives rise to the force constant density $f_{\alpha,\beta}(\varepsilon, i, j)$ which is plotted in Fig. 3(b) represented by the colored areas with dashed outline [the same quantity is also plotted in panels (c), (d), (e), and (f)]. As can be seen, $f_{x,z}(\varepsilon, i, j)$ is equal to $-f_{z,x}(\varepsilon, i, j)$ at any given energy within the numerical round up of 0.01 Å^{-2}. The y component of eDMI vector $\mathcal{D}(i, j)$ is thus derived from the nonzero antisymmetric force constants density $f_{z,x} - f_{x,z} \neq 0$ [defined in Eq. (9)] that is corresponding to the numerical results in Eq. (11). We are going to use the orbital-resolved force constant density $\xi^{m,n}_{\alpha,\beta}$ to understand the microscopic orbital origin of such eDMI vector. More specifically, it is going to be seen that the commutation between orbitals m and n on sites i and j gives rise to the inverse off-diagonal force constant density component, $\xi^{m,n}_{x,z} = -\xi^{n,m}_{z,x}$, which is symmetry protected. The relation of $f_{x,z} = -f_{z,x}$ in Fig. 3(b) can thus be understood since $f_{x,z} = \sum_{m,n} \xi^{m,n}_{x,z}$ and $f_{z,x} = \sum_{n,m} \xi^{n,m}_{z,x}$ according to Eq. (5), which explains the microscopic origin of the existence of the eDMI vector along the y axis [see Eq. (9)].

Considering two $PbTiO_3$ unit cells as depicted in Fig. 4(a), the two titanium atoms (blue balls on sites i and j) and their intermediate oxygen atom (red ball on site k) are displaced along the negative and positive z direction, respectively. Orbitals m and n of the two titanium sites are chosen from the $4s^1, 3p^3$, and $3d^5$ orbitals as listed in Fig. 4(b) to calculate the orbital-resolved force constant density $\xi^{m,n}_{\alpha,\beta}$. (Note that the inner core electrons such as $1s, 2s, 3s$, and $2p$ orbitals are treated as tightly bond to the nucleus and thus only give rise to the symmetric part of the force constants.) More specifically, according to Eq. (6), the expression of $\xi^{m,n}_{x,z}$ can be written as $\langle m, i|U_{i,x}\hat{G}^0 U_{j,z}|n, j\rangle$ [illustrated in Fig. 4(c1)] times $\langle n, j|\hat{G}^0|m, i\rangle$ [illustrated in Fig. 4(c2)]. In both Figs. 4(c1) and 4(c2), mirror m_{yz} [vertical lines as also indicated in (a) as vertical blue plane] operations are performed. Consequently, in Fig. 4(c1), the following functions are transformed: (1) orbital m on site i (left yellow circle) and orbital n on site j (right yellow square) are transformed to, in Fig. 4(d1), site j on the right and site i on the left, respectively; (2) effective perturbation potential $U_{i,x}$ on site i (left black arrow) and $U_{j,z}$ on site j (right black arrow) are transformed to, in Fig. 4(d1), $-U_{j,x}$ on site j (right red arrow) and $U_{i,z}$ on site i (left black arrow), respectively; (3) G^0 (green triangle) is unchanged since it is defined by the eigenfunctions of the unperturbed H^0 and follows the same crystalline symmetry, $P4mm$, as in the case of $PbTiO_3$ in Fig. 4(a). Note that symmetry operations should never alternate the integration values; thus we have proved that $\langle m, i|U_{i,x}\hat{G}^0 U_{j,z}|n, j\rangle$ [illustrated in Fig. 4(c1)] is equal to $-\langle n, i|U_{i,z}\hat{G}^0 U_{j,x}|m, j\rangle$ [illustrated in Fig. 4(d1)]. Employing the same three transformation rules of the functions to panels (c2) and (d2), the following relations can also be proved: $\langle n, j|\hat{G}^0|m, i\rangle$ in Fig. 4(c2) is equal to $\langle m, j|\hat{G}^0|n, i\rangle$ in Fig. 4(d2). Interestingly, the transformed expression, as illustrated in Figs. 4(d1) and 4(d2), is exactly the expression of $-\xi^{n,m}_{z,x}$, which means that $\xi^{m,n}_{x,z} = -\xi^{n,m}_{z,x}$ and $f_{x,z} = -f_{z,x}$ are constrained by the existence of the symmetry operation m_{yz}. One should notice that both orbitals m and n can be odd functions under the mirror operation m_{yz} and give rise to minus signs; e.g., p_x can be transformed to $-p_x$, d_{xz} can be transformed to $-d_{xz}$, and d_{xy} can be transformed to $-d_{xy}$. However, there are always two m orbitals and two n orbitals in the multiplication between $\langle m, i|U_{i,\alpha}\hat{G}^0 U_{j,\beta}|n, j\rangle$ and $\langle n, j|\hat{G}^0|m, i\rangle$, which means no minus sign in total can be given to $\xi^{m,n}_{\alpha,\beta}$ due to the transformation of orbitals m and n. Moreover, not all the orbitals m and n can contribute to nonzero orbital-resolved force constant density $\xi^{m,n}_{\alpha,\beta}$ and eDMI vector. The symmetry of orbitals m and n decides if certain electron hopping channels are allowed to give rise to nonzero eDMI vector. Taking the structure in Fig. 4(a) for example, if one orbital is even (e.g., $m = d_{x^2-y^2}$) and the other is odd (e.g., $n = d_{xy}$) under the operation of mirror m_{xz}, the orbital-resolved force constant density will be zero ($\xi^{m,n}_{x,z} = \xi^{n,m}_{z,x} = 0$) (see Sec. V of the Supplemental Material [43] for the proof from symmetry analysis and Fig. 1 of the Supplemental Material [43] for the numerical results).

The antisymmetric feature from the symmetry analysis is consistent with the numerical results as in Figs. 3(c)–3(f), where the red curve and blue curve are always in inverse sign. More specifically, Fig. 3(c) shows $\xi^{d_{xz},d_{xz}}_{x,z} =$

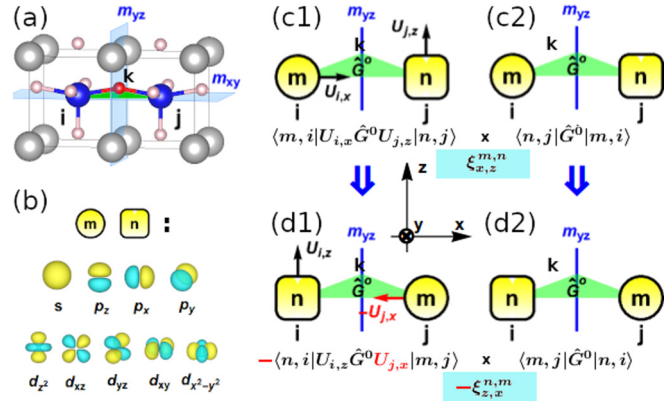

FIG. 4. (a) Two $PbTiO_3$ ($P4mm$ phase) unit cells along the x direction. The two blue balls on sites i and j are titanium atoms, and their intermediate oxygen atom is indicated by a red ball on site k. The vertical and horizontal blue planes represent mirrors m_{yz} and m_{xy}, respectively. A green triangle is used to indicate the relative displacements between the two titanium atoms and their intermediate oxygen atom. Panel (b) shows all the orbitals m and n in the orbital-resolved force constant expression. Expression of $\xi^{m,n}_{x,z}$ is sketched by a multiplication between the expressions in (c1) and (c2). The blue vertical lines in (c1) and (c2) are mirror m_{yz} operations and transform the expressions in (c1) and (c2) to the expressions in (d1) and (d2), respectively, and whose multiplication gives rise to $-\xi^{n,m}_{z,x}$. In all the expression sketches, the yellow circles and squares represent orbital m and n, respectively, the arrows are used to indicate effective perturbation potentials, and the green triangles [as also indicated in (a) among sites i, j, and k] are for Green's function $\hat{G}^0$.

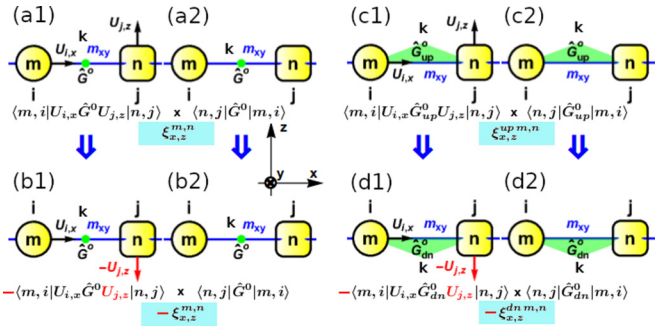

FIG. 5. If sites i, j, and k in Fig. 4(a) are collinear, expression of $\xi_{x,z}^{m,n}$ is sketched by a multiplication between expressions in (a1) and (a2). The blue horizontal lines in (a1) and (a2) are mirror m_{xy} operations and transform the expressions in (a1) and (a2) to the expressions in (b1) and (b2), respectively, and whose multiplication gives rise to $-\xi_{x,z}^{m,n}$. When site k is on top of sites i and j in the triangle, the expression of $\xi_{x,z}^{up,m,n}$ for such case is sketched by a multiplication between (c1) and (c2) which can be transformed by mirror m_{xy} (blue horizontal lines) to the expressions in (d1) and (d2) whose multiplication gives rise to $-\xi_{x,z}^{dn,m,n}$ which is for the case that site k is below sites i and j. In all the expression sketches, the yellow circles and squares represent orbital m and n, respectively, the arrows are used to indicate effective perturbation potentials, and the green dots and triangles are for Green's function $\hat{G}^0$.

$-\xi_{z,x}^{d_{xz},d_{xz}}$, Fig. 3(d) shows $\xi_{x,z}^{d_{x^2-y^2},d_{xz}} = -\xi_{z,x}^{d_{xz},d_{x^2-y^2}}$, Fig. 3(e) shows $\xi_{x,z}^{d_{xz},d_{z^2}} = -\xi_{z,x}^{d_{z^2},d_{xz}}$, and Fig. 3(f) shows $\xi_{x,z}^{d_{x^2-y^2},d_{z^2}} = -\xi_{z,x}^{d_{z^2},d_{x^2-y^2}}$. Figure 3(b) sums up the orbital-resolved force constant densities $\xi_{x,z}^{m,n}$ and $\xi_{z,x}^{n,m}$ that are in Figs. 3(c)–3(f) (red and blue solid lines). We can see that the total force constant densities $f_{x,z}$ and $f_{z,x}$ (colored area with dashed outline) are relatively well reproduced in Fig. 3(b). Contributions from other orbitals are relatively small or zero and can be found in Fig. 1 of the Supplemental Material [43]. Figure 3(g) explains why the d orbitals contribute most of the force constants. We can see that the DOS projected on the titanium atom is in the same energy region as nonzero force constant density [colored areas in Fig. 3(b)] and some peaks are also consistent, e.g., peaks at −3.5, −5.5, and −7.2 eV. The reason that the unoccupied titanium d orbitals have contributed to DOS under the Fermi level is due to the p-d interactions between titanium atoms [blue balls in the inset of panel (g)] and their intermediate oxygen atom [red ball in the inset of panel (g)], which can be seen in Fig. 3(h) where the DOS projected on the intermediate oxygen atom roughly has the same shapes as the DOS projected on the titanium atom in Fig. 3(g).

C. Local inversion-symmetry breaking and eDMI

The intermediate oxygen plays an essential role in the indirect interaction between the nearest-neighbor titanium atoms and so in the eDMI. For instance, in Fig. 5(a), when the intermediate oxygen (site k) is collinear with the two nearest-neighbor titanium atoms (sites i and j), the orbital-resolved force constant density $\xi_{x,z}^{m,n}$ can be proved to be always zero. Following similar transformation rules to those in Fig. 4, a mirror operation m_{xy} [blue horizontal line in Figs. 5(a1) and 5(a2)] reverses only the sign in the front of the $U_{j,z}$ (black vertical arrow on site j) in (a1) and results in $-\langle m, i|U_{i,x}\hat{G}^0 U_{j,z}|n, j\rangle$ in (b1), which indicates that $\xi_{x,z}^{m,n} = -\xi_{x,z}^{m,n}$ and $\xi_{x,z}^{m,n}$ has to be zero. Thus we have proved that breaking such mirror symmetry (by forming a triangle among sites i, j, and k) decides if eDMI exists, which is going to be another important rule in the "orbital selection rules" section. Note that such mirror-symmetry breaking (by forming a triangle) will result in a local-inversion-symmetry breaking (inversion center on the middle point between sites i and j) automatically. However, breaking such local inversion symmetry does not always give rise to mirror-symmetry breaking. For example, site k can be displaced along the line that connects sites i and j and away from the middle point between sites i and j, but eDMI is still forbidden because of the existence of mirror m_{xy} (see Fig. 5).

More importantly, Fig. 5 has also proved that the direction of the displacement of the site k with respect to sites i and j decides the direction of the eDMI vector. For instance, Figs. 5(c) and 5(d) prove that $\xi_{x,z}^{up,m,n} = -\xi_{x,z}^{dn,m,n}$, where $\xi_{x,z}^{up,m,n}$ is the orbital-resolved force constants density for the case that the site k is displaced along the positive z direction [green triangles in panels (c1) and (c2)] and $\xi_{x,z}^{dn,m,n}$ is the orbital-resolved force constant density for the case that the site k is displaced along the negative z direction [green triangles in panels (d1) and (d2)]. More specifically, in Figs. 5(c1) and 5(c2), the mirror m_{xy} (horizontal blue lines) (1) transforms the $\hat{G}_{up}^0$ (corresponding the $P4mm$ phase of $PbTiO_3$ with polarization along negative z direction) into the $\hat{G}_{dn}^0$ (corresponding to the $P4mm$ phase of $PbTiO_3$ with polarization along positive z direction) in (d1) and (d2), (2) transforms the $U_{j,z}$ in (c1) (vertical black arrow on site i) into the $-U_{j,z}$ in (d1) (vertical red arrow on site j), and (3) changes no other functions. Thus the $\xi_{x,z}^{up,m,n}$ defined by the multiplication between the expression in (c1) and (c2) is proved to be equal to $-\xi_{x,z}^{dn,m,n}$ defined by the multiplication between the expression in (d1) and (d2). In addition to $\xi_{x,z}^{up,m,n} = -\xi_{x,z}^{dn,m,n}$, we have already known that (1) the $\boldsymbol{\mathcal{D}}(i, j)$ vector in the $P4mm$ phase of $PbTiO_3$ is proportional to $(0, -F_{xz}, 0)$ and (2) $F_{xz} = \sum_{m,n}\int \xi_{x,z}^{m,n}(\varepsilon, i, j)d\varepsilon$. Thus $\boldsymbol{\mathcal{D}}^{up}(i, j) = -\boldsymbol{\mathcal{D}}^{dn}(i, j)$ can be proved, where $\boldsymbol{\mathcal{D}}^{up}$ is eDMI vector in the case that the intermediate oxygen site displaced along the positive z direction and $\boldsymbol{\mathcal{D}}^{dn}$ is eDMI vector in the case that intermediate oxygen site displaced along the negative z direction. Such conclusion explains why the $\boldsymbol{\mathcal{D}}(i, j)$ vector is not homogeneous in some perovskite oxides [32], for example, with oxygen octahedral tilting where the oxygen atoms are displaced alternatively along positive and negative z direction.

In Fig. 4(c1), we have also noticed that the inverse feature between the off-diagonal components of the force constant density (antisymmetric in force constants) $f_{x,z} = -f_{z,x}$ is due to the fact that under the m_{yz} operation one effective perturbation potential, $U_{i,x}$ (black arrow), that is perpendicular to m_{yz} on site i changes sign and the other $U_{j,z}$ (black arrow) that is parallel to m_{yz} on site j does not. Such condition seems also satisfied by $U_{i,x}$ (vector perpendicular to m_{yz}) and $U_{j,y}$ (vector parallel to m_{yz}), which is corresponding to the the antisymmetric feature between force constants density $f_{x,y} = -f_{y,x}$. However, $f_{x,y} = -f_{y,x} = 0$ can be further proved by the

symmetry operation of mirror m_{xz} that goes through sites i, j, and k (see Sec. V of the Supplemental Material [43]). This is also consistent with the results of the force constant calculations in Eq. (11). On the other hand, neither $U_{i,y}$ (vector parallel to m_{yz}) and $U_{j,z}$ (vector parallel to m_{yz}) nor $U_{i,z}$ (vector parallel to m_{yz}) and $U_{j,y}$ (vector parallel to m_{yz}) change sign under mirror m_{yz}; thus the off-diagonal components (in the y and z directions) of the force constant density is only symmetric, $f_{y,z} = f_{z,y}$, and thus does not give rise to any eDMI. Taking consideration of $f_{yz} = f_{zy} = 0$, $f_{zx} = -f_{xz}$, and $f_{xy} = f_{yx}$ into Eq. (7), we can see that the only nonzero eDMI vector component is along the y axis which is perpendicular to the (i, j, k) plane. This is going to be one important rule in the "orbital selection rules" section to be discussed below.

D. eDMI with tiltings

So far we have noticed one important fact about eDMI: it comes from the indirect interaction between the nearest-neighbor titanium sites through the displaced intermediate oxygen site in $PbTiO_3$, which suggests that eDMI is at least a three-body (indirect) interaction. As a matter of fact and as can be seen from Fig. 4(a) and Fig. 5, the relative displacement of the intermediate site k along the z direction is critical to give nonzero antisymmetric force constants. It is consistent with the phenomenological model in Eq. (12), in which the $\boldsymbol{u}_i + \boldsymbol{u}_j$ includes the relative displacement of the intermediate oxygen with respect to titanium sites i and j. Such relative displacement can be seen from an equivalent expression in Eq. (44) of the Supplemental Material [43] which is written in an atomistic displacement basis which can be seen as expanding the polar mode $\boldsymbol{u}$ with the displacements ($\boldsymbol{\mu B}$) of titanium cations and their surrounding oxygen anions (O(X) in [100], O(Y) in [010], and O(Z) in [001] directions with respect to the titanium cations in Fig. 5(b) of the Supplemental Material [43]). [As indicated in Fig. 1(a), the polar mode $\boldsymbol{u}$ consists of titanium cations moving in one direction with respect to the oxygen anions that are on the side of titanium ions within (001) planes being moved toward the opposite direction.] Equation (44) of the Supplemental Material [43] tells us that the displacements of intermediate oxygen ($\boldsymbol{\mu X}$, $\boldsymbol{\mu Y}$, and $\boldsymbol{\mu Z}$ in Eq. (44) of the Supplemental Material [43]) or equivalently polar modes $\boldsymbol{u}_i + \boldsymbol{u}_j$ [in Eq. (12) of the main text] that are normal to $\boldsymbol{e}_{ij}$ will give rise to a nonzero contribution to the eDMI energy. On the other hand, if the local inversion-symmetry breaking is from the intermediate oxygen that is displaced parallel to the line that connects sites i and j or equivalently $(\boldsymbol{u}_i + \boldsymbol{u}_j) \times \boldsymbol{e}_{ij} = 0$, the eDMI vector is always zero, as has been proven by Fig. 5.

Interestingly, such displacement of the intermediate oxygen site can also be associated with oxygen octahedral rotations in some perovskite materials, which is therefore consistent with a recent finding that the eDMI vector can be related to such rotations [32]. More specifically, in a case with the oxygen octahedra tilting pattern as in Fig. 6, the intermediate oxygen O1(X) that locates at position $\boldsymbol{r}_1 = \boldsymbol{R}_1 + (0.5, 0, 0)$ between titanium atoms in cells $\boldsymbol{R}_1 = (-1, 0, 0)$ and $\boldsymbol{R}_2 = (0, 0, 0)$ is displaced relatively upward $[\boldsymbol{\mu X}(\boldsymbol{r}_1) > 0]$ and the intermediate oxygen O2(X) that locates at position $\boldsymbol{r}_2 = \boldsymbol{R}_2 + (0.5, 0, 0)$ between titanium atoms in cells $\boldsymbol{R}_2 = (0, 0, 0)$ and $\boldsymbol{R}_3 = (1, 0, 0)$ is displaced relatively

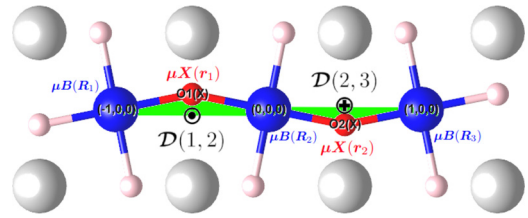

FIG. 6. Illustration plot of the crystal structure with oxygen octahedral tiltings. Three 5-atom cells along [100] direction are plotted. The cell indexes are marked on the titanium atoms (blue ball) as $\boldsymbol{R}_1 = (-1, 0, 0)$, $\boldsymbol{R}_2 = (0, 0, 0)$, and $\boldsymbol{R}_3 = (1, 0, 0)$, respectively. Note that the atomistic basis is defined in a unit cell in which the titanium atom locates at the origin (0,0,0) (see Fig. 5(a) of the Supplemental Material [43]). Thus the oxygen atoms O1(X) and O2(X) site at positions $\boldsymbol{r}_1 = \boldsymbol{R}_1 + (0.5, 0, 0)$ and $\boldsymbol{r}_2 = \boldsymbol{R}_2 + (0.5, 0, 0)$ before the octahedra tilting displacements, respectively. The oxygen octahedra tiltings around titanium atoms in cells $\boldsymbol{R}_1$, $\boldsymbol{R}_2$, and $\boldsymbol{R}_3$ are anticlockwise, clockwise, and anticlockwise, respectively. Note that the atomic displacement variables for titanium atom ($\boldsymbol{\mu B}$) and oxygen atom along [100] directions ($\boldsymbol{\mu X}$) are labeled and their definition in unit cell can be found in Fig. 5(a) of the Supplemental Material [43]. Note also that we use $\boldsymbol{R}$ for cell index and $\boldsymbol{r}$ for atom position in this paper.

downward $[\boldsymbol{\mu X}(\boldsymbol{r}_2) < 0]$. Thus two triangles (green in Fig. 6) are formed: (1) an upward-oriented triangle among the titanium atom in cell $\boldsymbol{R}_1 = (-1, 0, 0)$, titanium atom in $\boldsymbol{R}_2 = (0, 0, 0)$, and oxygen atom O1($X$) at position $\boldsymbol{r}_1 = \boldsymbol{R}_1 + (0.5, 0, 0)$, and (2) a downward-oriented triangle among the titanium atom in cell $\boldsymbol{R}_2 = (0, 0, 0)$, titanium atom in $\boldsymbol{R}_3 = (1, 0, 0)$, and oxygen atom O2($X$) at position $\boldsymbol{r}_2 = \boldsymbol{R}_2 + (0.5, 0, 0)$. According to Eq. (44) of the Supplemental Material [43] [which is the equivalent expression of Eq. (12) of the main text but written in atomistic basis], the eDMI vector $\mathcal{D}(1, 2)$ between $\boldsymbol{R}_1 = (-1, 0, 0)$ and $\boldsymbol{R}_2 = (0, 0, 0)$ (up-triangle case) is proportional to $\boldsymbol{\mu X}(\boldsymbol{r_1}) \times \boldsymbol{e}_{ij} = (0, \mu X_z(\boldsymbol{r}_1), -\mu X_y(\boldsymbol{r}_1))$ and the eDMI vector $\mathcal{D}(2, 3)$ between $\boldsymbol{R}_2 = (0, 0, 0)$ and $\boldsymbol{R}_3 = (1, 0, 0)$ (down-triangle case) is proportional to $\boldsymbol{\mu X}(\boldsymbol{r_2}) \times \boldsymbol{e}_{ij} = (0, \mu X_z(\boldsymbol{r}_2), -\mu X_y(\boldsymbol{r}_2))$. Thus $\mathcal{D}(1, 2)$ is along the [010] direction and $\mathcal{D}(2, 3)$ is along the [0-10] direction, considering that $\mu X_z(\boldsymbol{r}_1) > 0$, $\mu X_z(\boldsymbol{r}_2) < 0$, and $\mu X_y(\boldsymbol{r}_1) = \mu X_y(\boldsymbol{r}_2) = 0$ in the tilting motions in Fig. 6, which is consistent with our discussion in Figs. 5(c) and 5(d) and, more importantly, reproduces the alternatively changed $\boldsymbol{\mathcal{D}}$ vectors due to oxygen octahedral tiltings as in Ref. [32].

Thus our microscopic description presents a general explanation of the eDMI that is suitable to ferroelectric materials with or without oxygen octahedral tiltings. Note that Eq. (12) further implies that the eDMI vector can be induced by other effects, such as polar motions. In fact, we perform DFT calculations that show that there can be noncollinear polar texture without the help of oxygen octahedral tiltings (see Sec. VII of the Supplemental Material [43]).

E. Orbital selection rules of eDMI

Based on the conclusions we made by the symmetry analysis as we derived the microscopic origin of eDMI in Figs. 4 and 5, selection rules can be summarized in order to determine

TABLE I. Orbital selection rules of the electric Dzyaloshinskii-Moriya interaction in the case of three sites. The two rules are shown in the bottom of the table. In the sketch of rule 1, the i, j, and k are used to indicate the three ionic sites, m_1 is a mirror that goes through k site and is perpendicular to the line connecting i and j sites, and m_3 is a mirror that goes through all i, j, and k sites. The table includes the results when such three rules are applied when both orbitals m and n range over all s, p, and d orbitals. The check marks in the table indicate the nonzero orbital-resolved force constant density is in antisymmetric form $\xi^{m,n}_{x,z} = -\xi^{n,m}_{z,x} \neq 0$ and gives rise to the y component of eDMI vector.

	s	p_z	p_x	p_y	d_{z^2}	d_{xz}	d_{yz}	d_{xy}	$d_{x^2-y^2}$
s	✓	✓	✓		✓	✓			✓
p_z	✓	✓	✓		✓	✓			✓
p_x	✓	✓	✓		✓	✓			✓
p_y				✓				✓	
d_{z^2}	✓	✓	✓		✓	✓			✓
d_{xz}	✓	✓	✓		✓[c]	✓[a]			✓
d_{yz}							✓	✓	
d_{xy}				✓			✓	✓	
$d_{x^2-y^2}$	✓	✓	✓		✓[d]	✓[b]			✓

eDMI orbital selection rules

rule 1: noncollinear three orbitals

triangle: 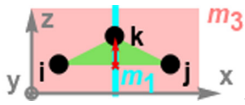

, $\mathcal{D}(i,j) \perp m_3$

rule 2: mirror m_3
the orbitals on sites i and j should be either
both even or both odd with respect to
the operation of mirror m_3.

[a]Plotted in Fig. 3(c).
[b]Plotted in Fig. 3(d).
[c]Plotted in Fig. 3(e).
[d]Plotted in Fig. 3(f).

what kind of orbital combinations can give rise to eDMI (see details in Sec. V of the Supplemental Material [43]). With such orbital selection rules together with the DOS of the material, we can address which orbitals are allowed and which orbitals possibly give rise to a quantitatively large eDMI, which makes engineering of eDMI possible. Two rules are summarized in Table I, assuming a three-site model in which i and j characterize cation sites (e.g., titanium atoms) and k is associated with the intermediate anion site (e.g., oxygen atom) located in the middle of sites i and j: (1) the local inversion symmetry should be broken by the k-site displacement that is off the line that goes through i and j sites, and thus a triangle is formed; (2) the orbitals on sites i and j should be either both even or both odd with respect to the mirror that goes through all three sites. Satisfying the two rules, the eDMI $\mathcal{D}$ vector will exist and has to be perpendicular to the triangle formed by sites i, j, and k. In rule (1), not all the local inversion-symmetry breakings give rise to an eDMI vector. As a matter of fact, while there are two ways to break the local inversion symmetry, namely (i) site k is displaced away from the line that connects sites i and j, and (ii) site k is displaced along the line that connects sites i and j, the second way does not give rise to eDMI because, as proven in Figs. 5(a) and 5(b), the orbital-resolved force constant density $\xi^{m,n}_{\alpha,\beta}$ vanishes due to the existence of mirror m_{xy}. Extended tables that explain all the symmetry analysis (that are needed for summarizing Table I) are indicated in Appendix A of the Supplemental Material [43]. Following eDMI orbital selection rules, all eDMI activated orbital combinations that involve s, p, and d orbitals are derived and listed in Table I. For instance, the main contributions to eDMI of $PbTiO_3$ from $\xi^{m,n}_{x,z}$ and $\xi^{n,m}_{z,x}$ as discussed in Figs. 3(c)–3(f) can also be found in Table I, the check marks labeled by c, d, e, and f, respectively. Note that Table I is also confirmed by our numerical results involving these s, p, and d orbitals (see Secs. IV and V and Fig. 1 of the Supplemental Material [43]).

V. FURTHER REMARKS

In this work, we discuss an overlooked intrinsic dipolar interaction (eDMI) that could give chiral polar structures. However, there are other energy terms and extrinsic conditions that compete with such kind of coupling term, which could result in that (1) noncollinear textures are metastable high-energy phases, such as the Bloch component in the domain walls (high-energy defects) [30,88–90]; (2) only a narrow region in the phase diagram (with respect to temperature, strain, and even external electric field) shows nontrivial topological polar texture, also similar to the magnetic situations [14,91]; and (3) hidden phases corresponding to such kind of coupling could exist under external probes [92], such as laser pulses.

Based on the arguments provided in this paper, the eDMI should have no direct relation to the origin of the polar instability. Consequently, eDMI may also exist in different types of ferroelectrics (e.g., hyperferroelectrics, geometric/steric ferroelectrics, and even ferroelectric metals) if there are no other mechanisms/constraints forbidding it.

Note that the original effective Hamiltonian method [58] considers up to the second order for polar-polar interaction between cells, which gives rise to only a symmetric force constant matrix, unlike what the DFPT calculations tell us. The Ginzburg term in the phase field model [65] (Ginzburg-Landau-Devonshire theory [44–46]) obviously cannot reproduce antisymmetric force constants either which can be easily seen by realizing that the Ginzburg term is only the power of the gradient of polar modes. Consequently, our work should lead to revisiting currently used models.

It is also worth mentioning that our proposed microscopic theory for eDMI can be linked to several previous theoretical works. For example, the three-site model discussed in the present paper bears some analogy with the "triple-dipole-interaction" problem [93–95] among three neutral atoms (van der Waals–type interaction). Interestingly, the proposed Axilrod-Teller potential for this "triple-dipole interaction" can also give a nonzero antisymmetric part of the force constants, though the influence of the covalent bonding on the force constants was omitted (only polarization fluctuations were taken into account). In contrast, the study of the vibronic instability [96–98] of some crystals discussed the effects of covalent bonding but did not pay attention to the antisymmetric part of the force constants. We are also aware of a simple three-site LCAO model developed by Prosandeev *et al.* [99]

discussing the correlation of the local atomic displacements in perovskites. Such kind of correlations were earlier experimentally discovered from the diffuse scattering of neutrons in $KNbO_3$ [100,101].

VI. CONCLUSION

In conclusion, the microscopic origin of the electric Dzyaloshinskii-Moriya interaction is unveiled and discussed thanks to analytical analysis of the orbital-resolved force constant calculations. Our present study, therefore, emphasizes that eDMI exists and sheds some light onto its origin, which is that eDMI is an electron-mediated quantum effect in which (1) the local inversion-symmetry breaking activates previously forbidden electron hopping channels on adjacent atomic sites; and (2) the combination of the orbitals with particular symmetry (following eDMI orbital selection rules detailed in Table I) results in the electric Dzyaloshinskii-Moriya interaction. Though both eDMI and mDMI need electron hopping channels and local-inversion-symmetry breaking to occur, mDMI needs spin-orbit coupling to connect spin up and down, unlike eDMI. Thus eDMI naturally exists in polar materials because of the general existence of local-inversion-symmetry breaking. Moreover, eDMI energy is found to be at least third order in ionic displacements while mDMI energy "only" involves a second order in magnetic moments. Such differences may result in the formation of some exotic dipole textures that can differ from the extensively explored magnetic arrangements.

ACKNOWLEDGMENTS

The work is supported by ONR under Grant No. N00014-17-1-2818 (P.C. and L.B.), the Vannevar Bush Faculty Fellowship (VBFF) Grant No. N00014-20-1-2834 from the Department of Defense (H.J.Z. and L.B.), and the ARO Grant No. W911NF-21-1-0113. (L.B.). H.J.Z. and P.C. thank Prof. Wenhui Mi for the valuable discussions. The first-principles simulations and tight-binding calculations were done using the Arkansas High-Performance Computing Center.

[1] I. E. Dzyaloshinskii, Thermodynamic theory of weak ferromagnetism in antiferromagnetic substances, J. Exptl. Theoret. Phys. (U.S.S.R.) **32**, 1547 (1957) [Sov. Phys. JETP **5**, 1259 (1957)].

[2] I. Dzyaloshinsky, A thermodynamic theory of "weak" ferromagnetism of antiferromagnetics, J. Phys. Chem. Solids **4**, 241 (1958).

[3] T. Moriya, Anisotropic superexchange interaction and weak ferromagnetism, Phys. Rev. **120**, 91 (1960).

[4] N. R. Cooper, Propagating Magnetic Vortex Rings in Ferromagnets, Phys. Rev. Lett. **82**, 1554 (1999).

[5] C. Donnelly, K. L. Metlov, V. Scagnoli, M. Guizar-Sicairos, M. Holler, N. S. Bingham, J. Raabe, L. J. Heyderman, N. R. Cooper, and S. Gliga, Experimental observation of vortex rings in a bulk magnet, Nat. Phys. **17**, 316 (2021).

[6] T. Skyrme, A unified field theory of mesons and baryons, Nucl. Phys. **31**, 556 (1962).

[7] E. H. Aifer, B. B. Goldberg, and D. A. Broido, Evidence of Skyrmion Excitations about $\nu = 1n$-Modulation-Doped Single Quantum Wells by Interband Optical Transmission, Phys. Rev. Lett. **76**, 680 (1996).

[8] A. N. Bogdanov and U. K. Rößler, Chiral Symmetry Breaking in Magnetic Thin Films and Multilayers, Phys. Rev. Lett. **87**, 037203 (2001).

[9] U. K. Rößler, A. N. Bogdanov, and C. Pfleiderer, Spontaneous skyrmion ground states in magnetic metals, Nature (London) **442**, 797 (2006).

[10] S. Mühlbauer, B. Binz, F. Jonietz, C. Pfleiderer, A. Rosch, A. Neubauer, R. Georgii, and P. Böni, Skyrmion lattice in a chiral magnet, Science **323**, 915 (2009).

[11] X. Z. Yu, Y. Onose, N. Kanazawa, J. H. Park, J. H. Han, Y. Matsui, N. Nagaosa, and Y. Tokura, Real-space observation of a two-dimensional skyrmion crystal, Nature (London) **465**, 901 (2010).

[12] S. Heinze, K. von Bergmann, M. Menzel, J. Brede, A. Kubetzka, R. Wiesendanger, G. Bihlmayer, and S. Blügel, Spontaneous atomic-scale magnetic skyrmion lattice in two dimensions, Nat. Phys. **7**, 713 (2011).

[13] N. Romming, C. Hanneken, M. Menzel, J. E. Bickel, B. Wolter, K. von Bergmann, A. Kubetzka, and R. Wiesendanger, Writing and deleting single magnetic skyrmions, Science **341**, 636 (2013).

[14] N. Nagaosa and Y. Tokura, Topological properties and dynamics of magnetic skyrmions, Nat. Nanotechnol. **8**, 899 (2013).

[15] B. Dupé, M. Hoffmann, C. Paillard, and S. Heinze, Tailoring magnetic skyrmions in ultra-thin transition metal films, Nat. Commun. **5**, 4030 (2014).

[16] P.-J. Hsu, A. Kubetzka, A. Finco, N. Romming, K. von Bergmann, and R. Wiesendanger, Electric-field-driven switching of individual magnetic skyrmions, Nat. Nanotechnol. **12**, 123 (2017).

[17] R. Wiesendanger, Nanoscale magnetic skyrmions in metallic films and multilayers: A new twist for spintronics, Nat. Rev. Mater. **1**, 16044 (2016).

[18] S. Bera and S. S. Mandal, Theory of the skyrmion, meron, antiskyrmion, and antimeron in chiral magnets, Phys. Rev. Res. **1**, 033109 (2019).

[19] L. Du, A. Yang, A. V. Zayats, and X. Yuan, Deep-subwavelength features of photonic skyrmions in a confined electromagnetic field with orbital angular momentum, Nat. Phys. **15**, 650 (2019).

[20] J. Zang, V. Cros, and A. Hoffmann, *Topology in Magnetism* (Springer International Publishing, New York, 2018).

[21] P. Schoenherr, J. Müller, L. Köhler, A. Rosch, N. Kanazawa, Y. Tokura, M. Garst, and D. Meier, Topological domain walls in helimagnets, Nat. Phys. **14**, 465 (2018).

[22] A. K. Yadav, C. T. Nelson, S. L. Hsu, Z. Hong, J. D. Clarkson, C. M. Schlepütz, A. R. Damodaran, P. Shafer, E. Arenholz, L. R. Dedon, D. Chen, A. Vishwanath, A. M. Minor, L. Q. Chen, J. F. Scott, L. W. Martin, and R. Ramesh, Observation

of polar vortices in oxide superlattices, Nature (London) **530**, 198 (2016).

[23] Q. Zhang, L. Xie, G. Liu, S. Prokhorenko, Y. Nahas, X. Pan, L. Bellaiche, A. Gruverman, and N. Valanoor, Nanoscale bubble domains and topological transitions in ultrathin ferroelectric films, Adv. Mater. **29**, 1702375 (2017).

[24] S. Das, Y. Tang, Z. Hong, M. Gonçalves, M. McCarter, C. Klewe, K. Nguyen, F. Gómez-Ortiz, P. Shafer, E. Arenholz *et al.*, Observation of room-temperature polar skyrmions, Nature (London) **568**, 368 (2019).

[25] S.-L. Hsu, M. R. McCarter, C. Dai, Z. Hong, L.-Q. Chen, C. T. Nelson, L. W. Martin, and R. Ramesh, Emergence of the vortex state in confined ferroelectric heterostructures, Adv. Mater. **31**, 1901014 (2019).

[26] S. R. Bakaul, S. Prokhorenko, Q. Zhang, Y. Nahas, Y. Hu, A. Petford-Long, L. Bellaiche, and N. Valanoor, Freestanding ferroelectric bubble domains, Adv. Mater. **33**, 2105432 (2021).

[27] D. Rusu, J. J. P. Peters, T. P. A. Hase, J. A. Gott, G. A. A. Nisbet, J. Strempfer, D. Haskel, S. D. Seddon, R. Beanland, A. M. Sanchez, and M. Alexe, Ferroelectric incommensurate spin crystals, Nature (London) **602**, 240 (2022).

[28] I. I. Naumov, L. Bellaiche, and H. Fu, Unusual phase transitions in ferroelectric nanodisks and nanorods, Nature (London) **432**, 737 (2004).

[29] Y. Nahas, S. Prokhorenko, L. Louis, Z. Gui, I. Kornev, and L. Bellaiche, Discovery of stable skyrmionic state in ferroelectric nanocomposites, Nat. Commun. **6**, 8542 (2015).

[30] M. P. Gonçalves, C. Escorihuela-Sayalero, P. Garca-Fernández, J. Junquera, and J. Íñiguez, Theoretical guidelines to create and tune electric skyrmion bubbles, Sci. Adv. **5**, eaau7023 (2019).

[31] Z. Hong, A. R. Damodaran, F. Xue, S.-L. Hsu, J. Britson, A. K. Yadav, C. T. Nelson, J.-J. Wang, J. F. Scott, L. W. Martin, R. Ramesh, and L.-Q. Chen, Stability of polar vortex lattice in ferroelectric superlattices, Nano Lett. **17**, 2246 (2017).

[32] H. J. Zhao, P. Chen, S. Prosandeev, S. Artyukhin, and L. Bellaiche, Dzyaloshinskii-Moriya-like interaction in ferroelectrics and antiferroelectrics, Nat. Mater. **20**, 341 (2021).

[33] D. D. Khalyavin, R. D. Johnson, F. Orlandi, P. G. Radaelli, P. Manuel, and A. A. Belik, Emergent helical texture of electric dipoles, Science **369**, 680 (2020).

[34] M. Uchida, Y. Onose, Y. Matsui, and Y. Tokura, Real-space observation of helical spin order, Science **311**, 359 (2006).

[35] S. L. Zhang, I. Stasinopoulos, T. Lancaster, F. Xiao, A. Bauer, F. Rucker, A. A. Baker, A. I. Figueroa, Z. Salman, F. L. Pratt, S. J. Blundell, T. Prokscha, A. Suter, J. Waizner, M. Garst, D. Grundler, G. van der Laan, C. Pfleiderer, and T. Hesjedal, Room-temperature helimagnetism in FeGe thin films, Sci. Rep. **7**, 123 (2017).

[36] C. S. Perreault, Y. K. Vohra, A. M. dos Santos, and J. J. Molaison, Neutron diffraction study of magnetic ordering in high pressure phases of rare earth metal holmium, J. Magn. Magn. Mater. **507**, 166843 (2020).

[37] M. Pereiro, D. Yudin, J. Chico, C. Etz, O. Eriksson, and A. Bergman, Topological excitations in a kagome magnet, Nat. Commun. **5**, 4815 (2014).

[38] N. Gao, S. G. Je, M. Y. Im, J. W. Choi, M. Yang, Q. Li, T. Y. Wang, S. Lee, H. S. Han, K. S. Lee, W. Chao, C. Hwang, J. Li, and Z. Q. Qiu, Creation and annihilation of topological meron pairs in in-plane magnetized films, Nat. Commun. **10**, 5603 (2019).

[39] J. F. Scott, Multiferroic memories, Nat. Mater. **6**, 256 (2007).

[40] S. Luo and L. You, Skyrmion devices for memory and logic applications, APL Mater. **9**, 050901 (2021).

[41] M. Born, K. Huang, and M. Lax, Dynamical theory of crystal lattices, Am. J. Phys. **23**, 474 (1955).

[42] Quantitatively, there exists a unitary transformation between the force constants of ions and the force constants of polarizations. Such transformation matrix can be obtained by taking the eigenvectors from diagonalizing the force constant matrix of the $PbTiO_3$ cubic structure.

[43] See Supplemental Material at http://link.aps.org/supplemental/10.1103/PhysRevB.106.224101 for details on the discussion of two-body Coulomb interaction, derivation of orbital-resolved force constants, orbital selection rules of eDMI, derivation of the third-order form of eDMI, and effective Hamiltonian parameters.

[44] L. Landau, The theory of phase transitions, Nature (London) **138**, 840 (1936).

[45] V. Ginzburg, On the dielectric properties of ferroelectric (seignetteelectric) crystals and barium titanate, Zh. Eksp. Teor. Fiz. **15**, 739 (1945).

[46] V. Ginzburg, On polarization and piezoelectric effect of barium titanate near the point of ferroelectric transition, Zh. Eksp. Teor. Fiz. **19**, 36 (1949).

[47] R. P. Feynman, Forces in molecules, Phys. Rev. **56**, 340 (1939).

[48] F. J. Dyson, The *S* matrix in quantum electrodynamics, Phys. Rev. **75**, 1736 (1949).

[49] S. L. Adler, Quantum theory of the dielectric constant in real solids, Phys. Rev. **126**, 413 (1962).

[50] N. Wiser, Dielectric constant with local field effects included, Phys. Rev. **129**, 62 (1963).

[51] H. Hellmann, *Einführung in die Quantenchemie* (Franz Deuticke, Vienna, 1937).

[52] M. Born and V. Fock, Beweis des adiabatensatzes, Z. Phys. **51**, 165 (1928).

[53] M. Lannoo, A tight-binding derivation of force constants : Application to covalent systems, J. Phys. France **40**, 461 (1979).

[54] G. Moraitis, J. Khalifeh, and C. Demangeat, Tight-binding calculation of force constants in α palladium hydrides, J. Less-Common Met. **101**, 203 (1984).

[55] M. Elstner, D. Porezag, G. Jungnickel, J. Elsner, M. Haugk, T. Frauenheim, S. Suhai, and G. Seifert, Self-consistent-charge density-functional tight-binding method for simulations of complex materials properties, Phys. Rev. B **58**, 7260 (1998).

[56] E. N. Economou, *Green's Functions in Quantum Physics* (Springer-Verlag, Berlin, 2006).

[57] A. Szilva, M. Costa, A. Bergman, L. Szunyogh, L. Nordström, and O. Eriksson, Interatomic Exchange Interactions for Finite-Temperature Magnetism and Nonequilibrium Spin Dynamics, Phys. Rev. Lett. **111**, 127204 (2013).

[58] W. Zhong, D. Vanderbilt, and K. M. Rabe, First-principles theory of ferroelectric phase transitions for perovskites: The case of $BaTiO_3$, Phys. Rev. B **52**, 6301 (1995).

[59] S. Baroni, S. de Gironcoli, A. D. Corso, and P. Giannozzi, Phonons and related crystal properties from density-functional perturbation theory, Rev. Mod. Phys. **73**, 515 (2001).

[60] A. Liechtenstein, M. Katsnelson, V. Antropov, and V. Gubanov, Local spin density functional approach to the theory of exchange interactions in ferromagnetic metals and alloys, J. Magn. Magn. Mater. **67**, 65 (1987).

[61] S. Lounis and P. H. Dederichs, Mapping the magnetic exchange interactions from first principles: Anisotropy anomaly and application to Fe, Ni, and Co, Phys. Rev. B **82**, 180404(R) (2010).

[62] X. He, N. Helbig, M. J. Verstraete, and E. Bousquet, TB2j: A python package for computing magnetic interaction parameters, Comput. Phys. Commun. **264**, 107938 (2021).

[63] P. Chen, H. Zhao, S. Artyukhin, and L. Bellaiche, LINVARIANT, https://github.com/PaulChern/LINVARIANT.

[64] B. J. Campbell, H. T. Stokes, D. E. Tanner, and D. M. Hatch, ISODISPLACE: A web-based tool for exploring structural distortions, J. Appl. Crystallogr. **39**, 607 (2006).

[65] L.-Q. Chen, Phase-field method of phase transitions/domain structures in ferroelectric thin films: A review, J. Am. Ceram. Soc. **91**, 1835 (2008).

[66] O. Besbes, S. Nikolaev, N. Meskini, and I. Solovyev, Microscopic origin of ferromagnetism in the trihalides $CrCl_3$ and CrI_3, Phys. Rev. B **99**, 104432 (2019).

[67] R. Cardias, A. Bergman, A. Szilva, Y. O. Kvashnin, J. Fransson, A. B. Klautau, O. Eriksson, and L. Nordström, Dzyaloshinskii-Moriya interaction in absence of spin-orbit coupling, arXiv:2003.04680.

[68] R. Cardias, A. Szilva, M. Bezerra-Neto, M. Ribeiro, A. Bergman, Y. O. Kvashnin, J. Fransson, A. Klautau, O. Eriksson, and L. Nordström, First-principles Dzyaloshinskii-Moriya interaction in a non-collinear framework, Sci. Rep. **10**, 20339 (2020).

[69] R. Sakuma, Symmetry-adapted Wannier functions in the maximal localization procedure, Phys. Rev. B **87**, 235109 (2013).

[70] G. Pizzi, V. Vitale, R. Arita, S. Blügel, F. Freimuth, G. Géranton, M. Gibertini, D. Gresch, C. Johnson, T. Koretsune, J. Ibañez-Azpiroz, H. Lee, J.-M. Lihm, D. Marchand, A. Marrazzo, Y. Mokrousov, J. I. Mustafa, Y. Nohara, Y. Nomura, L. Paulatto *et al.*, Wannier90 as a community code: New features and applications, J. Phys.: Condens. Matter **32**, 165902 (2020).

[71] P. Giannozzi, S. Baroni, N. Bonini, M. Calandra, R. Car, C. Cavazzoni, D. Ceresoli, G. L. Chiarotti, M. Cococcioni, I. Dabo, A. D. Corso, S. de Gironcoli, S. Fabris, G. Fratesi, R. Gebauer, U. Gerstmann, C. Gougoussis, A. Kokalj, M. Lazzeri, L. Martin-Samos *et al.*, QUANTUM ESPRESSO: A modular and open-source software project for quantum simulations of materials, J. Phys.: Condens. Matter **21**, 395502 (2009).

[72] P. Giannozzi, O. Andreussi, T. Brumme, O. Bunau, M. B. Nardelli, M. Calandra, R. Car, C. Cavazzoni, D. Ceresoli, M. Cococcioni, N. Colonna, I. Carnimeo, A. D. Corso, S. de Gironcoli, P. Delugas, R. A. DiStasio, Jr., A. Ferretti, A. Floris, G. Fratesi, G. Fugallo *et al.*, Advanced capabilities for materials modelling with Quantum ESPRESSO, J. Phys.: Condens. Matter **29**, 465901 (2017).

[73] D. R. Hamann, Optimized norm-conserving Vanderbilt pseudopotentials, Phys. Rev. B **88**, 085117 (2013).

[74] Wikipedia contributors, Antisymmetric exchange, in Wikipedia, the free encyclopedia.

[75] F. Keffer, Moriya interaction and the problem of the spin arrangements in βMnS, Phys. Rev. **126**, 896 (1962).

[76] S.-W. Cheong and M. Mostovoy, Multiferroics: A magnetic twist for ferroelectricity, Nat. Mater. **6**, 13 (2007).

[77] Such transformation matrix can be obtained by taking the eigenvectors from diagonalizing the force constant matrix of the $PbTiO_3$ cubic structure.

[78] H. J. Zhao, P. Chen, S. Prosandeev, C. Paillard, K. Patel, J. Íñiguez, and L. Bellaiche, Energetic couplings in ferroics, Adv. Electron. Mater. **8**, 2100639 (2021).

[79] K. C. Erb and J. Hlinka, Vector, bidirector, and Bloch skyrmion phases induced by structural crystallographic symmetry breaking, Phys. Rev. B **102**, 024110 (2020).

[80] H. Katsura, N. Nagaosa, and A. V. Balatsky, Spin Current and Magnetoelectric Effect in Noncollinear Magnets, Phys. Rev. Lett. **95**, 057205 (2005).

[81] A. Raeliarijaona, S. Singh, H. Fu, and L. Bellaiche, Predicted Coupling of the Electromagnetic Angular Momentum Density with Magnetic Moments, Phys. Rev. Lett. **110**, 137205 (2013).

[82] F. N. Rybakov, A. B. Borisov, S. Blügel, and N. S. Kiselev, New Type of Stable Particlelike States in Chiral Magnets, Phys. Rev. Lett. **115**, 117201 (2015).

[83] A. S. Ahmed, J. Rowland, B. D. Esser, S. R. Dunsiger, D. W. McComb, M. Randeria, and R. K. Kawakami, Chiral bobbers and skyrmions in epitaxial FeGe/Si(111) films, Phys. Rev. Mater. **2**, 041401(R) (2018).

[84] F. Zheng, F. N. Rybakov, A. B. Borisov, D. Song, S. Wang, Z.-A. Li, H. Du, N. S. Kiselev, J. Caron, A. Kovács, M. Tian, Y. Zhang, S. Blügel, and R. E. Dunin-Borkowski, Experimental observation of chiral magnetic bobbers in B20-type FeGe, Nat. Nanotechnol. **13**, 451 (2018).

[85] M. Redies, F. R. Lux, J.-P. Hanke, P. M. Buhl, G. P. Müller, N. S. Kiselev, S. Blügel, and Y. Mokrousov, Distinct magnetotransport and orbital fingerprints of chiral bobbers, Phys. Rev. B **99**, 140407(R) (2019).

[86] K. Ran, Y. Liu, Y. Guang, D. M. Burn, G. van der Laan, T. Hesjedal, H. Du, G. Yu, and S. Zhang, Creation of a Chiral Bobber Lattice in Helimagnet-Multilayer Heterostructures, Phys. Rev. Lett. **126**, 017204 (2021).

[87] D. Lee, R. K. Behera, P. Wu, H. Xu, Y. L. Li, S. B. Sinnott, S. R. Phillpot, L. Q. Chen, and V. Gopalan, Mixed Bloch-Néel-Ising character of 180° ferroelectric domain walls, Phys. Rev. B **80**, 060102(R) (2009).

[88] J. C. Wojdeł and J. Íñiguez, Ferroelectric Transitions at Ferroelectric Domain Walls Found from First Principles, Phys. Rev. Lett. **112**, 247603 (2014).

[89] Y. J. Wang, D. Chen, Y. L. Tang, Y. L. Zhu, and X. L. Ma, Origin of the Bloch-type polarization components at the 180° domain walls in ferroelectric $PbTiO_3$, J. Appl. Phys. **116**, 224105 (2014).

[90] Y. Wu, G. Liu, Z. Gao, H. He, and J. Deng, Dynamic dielectric properties of the ferroelectric ceramic $Pb(Zr_{0.95}Ti_{0.05})O_3$ in shock compression under high electrical fields, J. Appl. Phys. **123**, 244102 (2018).

[91] A. Neubauer, C. Pfleiderer, B. Binz, A. Rosch, R. Ritz, P. G. Niklowitz, and P. Böni, Topological Hall Effect in the *A* Phase of MnSi, Phys. Rev. Lett. **102**, 186602 (2009).

[92] X. Li, T. Qiu, J. Zhang, E. Baldini, J. Lu, A. M. Rappe, and K. A. Nelson, Terahertz field–induced ferroelectricity in quantum paraelectric $SrTiO_3$, Science **364**, 1079 (2019).

[93] B. Axilrod and E. Teller, Interaction of the van der Waals type between three atoms, J. Chem. Phys. **11**, 299 (1943).

[94] B. Axilrod, Triple-dipole interaction. I. Theory, J. Chem. Phys. **19**, 719 (1951).

[95] Y. S. Barash and V. L. Ginzburg, Some problems in the theory of van der Waals forces, Sov. Phys. Usp. **27**, 467 (1984).

[96] I. Bersuker, On the origin of ferroelectricity in perovskite-type crystals, Phys. Lett. **20**, 589 (1966).

[97] I. B. Bersuker and B. Vekhter, The vibronic theory of ferroelectricity, Ferroelectrics **19**, 137 (1978).

[98] I. B. Bersuker and V. Z. Polinger, *Vibronic Interactions in Molecules and Crystals* (Springer Science & Business Media, Berlin, 2012).

[99] S. A. Prosandeev, E. V. Vinnikov, and N. M. Nebogatikov, Influence of covalent effects on potential relief of atoms in oxides of the perovskite family of ABO_3 type, Ukrainian J. Phys. **34**, 87 (1989).

[100] R. Comès, M. Lambert, and A. Guinier, Désordre linéaire dans les cristaux (cas du silicium, du quartz, et des pérovskites ferroélectriques), Acta Crystallogr., Sect. A **26**, 244 (1970).

[101] R. Currat, R. Comes, B. Dorner, and E. Wiesendanger, Inelastic neutron scattering in orthorhombic $KNbO_3$, J. Phys. C: Solid State Phys. **7**, 2521 (1974).